Spin chirality driven tunability and multifunctionality in two-dimensional noncollinear antiferromagnets

Ting Lai,[1,2] Yongqian Zhu,[1,2] Jie Zhang,[1,2] Yuhui Li,[1,2] Guolin Wan,[1,2] Xudan Zhang,[1,2] Jia-Tao Sun,[3] Jinbo Pan,[1,2,*] and Shixuan Du[1,2,4,†]

[1]*Beijing National Laboratory for Condensed Matter Physics, Institute of Physics, Chinese Academy of Sciences, Beijing 100190, China*
[2]*University of Chinese Academy of Sciences, Chinese Academy of Sciences, Beijing 100190, China*
[3]*School of Integrated Circuits and Electronics, MIIT Key Laboratory for Low-Dimensional Quantum Structure and Devices, Beijing Institute of Technology, Beijing 100081, China*
[4]*Songshan Lake Materials Laboratory, Dongguan 523808, China*

(Received 30 April 2025; revised 17 April 2026; accepted 30 April 2026; published 12 June 2026)

Noncollinear antiferromagnets (NCAFs) offer an ideal platform for high-performance spintronic devices. Weak spin-orbit coupling (SOC) magnets, though abundant and important, are overlooked. We propose a symmetry framework for two-dimensional triangular antiferromagnets with 120° spin configurations, exploring multi-degree-of-freedom coexistence, coupling, and manipulation in the weak SOC regime. Symmetry analysis reveals the spin chirality driven ferroelectricity, Berry curvature, and antiferromagnetic-induced spin splitting—beyond magnetic or spin space group descriptions—coupled via an inversion-induced spin-chirality transformation. The coexistence and coupling of these properties remain regardless of the in-plane rotation of 120° spin configurations. Ferroelectric polarization reversal will switch spin chirality, Berry curvature, and spin splitting, enabling nonvolatile electric manipulation. Spin canting further breaks effective time-reversal symmetry, introducing unconventional SOC-independent valley polarization as an additional coupled degree of freedom. Multiple functionalities, including magnetoelectric coupling, circular dichroic Hall effect, nonrelativistic anisotropic Edelstein effect, and anomalous valley Hall effect, are enabled. High-throughput calculations on triangular-lattice MXenes identify monolayer $Zr_2VC_2X_2$ (X = F, Cl, Br, I) as promising candidates hosting 120° spin configurations. First-principles calculations exemplified by $Zr_2VC_2Cl_2$ validate the predicted tunability and multifunctionality. This work establishes a symmetry-guided framework for NCAF-based spintronic devices with tunable multifunctionality.

DOI: 10.1103/x52d-htvb

I. INTRODUCTION

Ferromagnetic (FM) materials have long dominated spintronics due to their net magnetization, enabling straightforward manipulation and detection [1]. Although this concept has facilitated widespread use, FM-based devices suffer from intrinsic drawbacks, such as large stray fields, susceptibility to perturbations, and relatively slow dynamics, limiting their performance [2,3]. In contrast, antiferromagnetic (AFM) materials offer promising alternatives with robustness against magnetic disturbances, negligible stray fields, and ultrafast dynamics. However, manipulating and detecting AFM states remain challenging, hindering information writing and reading.

Recent research has revealed that noncollinear antiferromagnets (NCAFs) hold promise for merging the benefits of both ferromagnets and antiferromagnets while mitigating their shortcomings [3]. The nontrivial Berry curvature enables electrical readout without net magnetization [4–7], and the spin-orbit torque facilitates efficient spin writing [8], as examples. With near-zero macroscopic magnetization, NCAFs eliminate stray field interference and resist perturbations, and their strong exchange interactions also allow fast terahertz-scale spin dynamics [9,10]. These properties make NCAFs an ideal platform for high-speed, high-density, nonvolatile, and low-power spintronic devices.

The noncollinear 120° spin configuration, known as Y-type antiferromagnetism (YAFM), is one of the most focused types of NCAFs, typically arising in kagome and triangular lattices composed of triangular plaquettes. Research on YAFM within kagome lattices has highlighted rich topological phenomena, such as the anomalous Hall effect and spin Hall effect [3,4,8,11], while studies on YAFM within triangular lattices have focused on type-II multiferroicity [12–16]. Despite this progress, significant gaps remain in the generation, control, and interplay of broader physical properties in NCAFs. At the same time, a unified symmetry-based framework for coupling and controlling multiple degrees of freedom has yet to be developed. Notably, magnets with weak SOC are vast and practically important [17] but largely neglected, as previous studies predominantly concentrated on strong-SOC magnets within a magnetic space group (MSG) [18–23] and SOC-free limit within a spin space group (SSG) [24–32]. Therefore, to capture the physical reality and multiple coupling effects

*Contact author: jbpan@iphy.ac.cn
†Contact author: sxdu@iphy.ac.cn

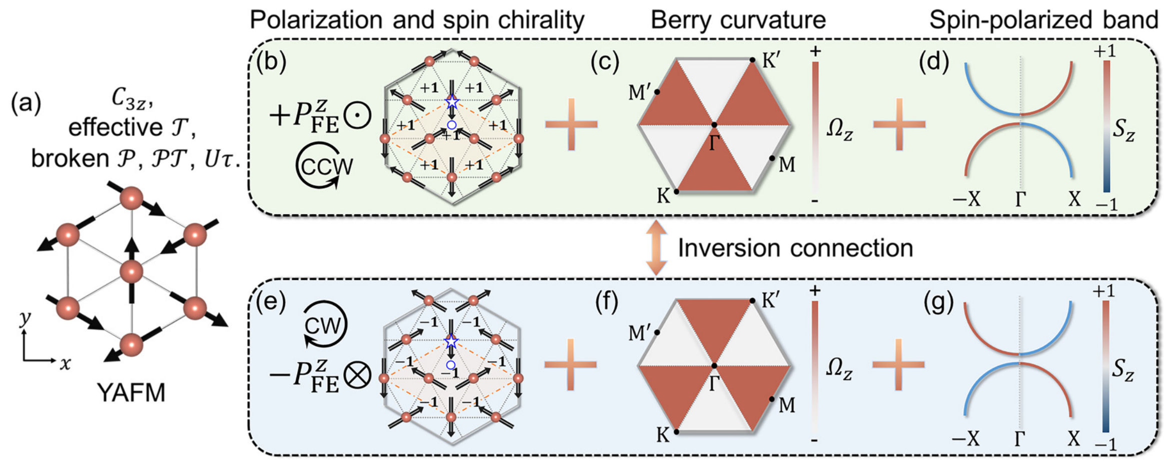

FIG. 1. Schematic of inversion-connected spin chirality, ferroelectricity, Berry curvature, and spin splitting in coplanar YAFM. (a) YAFM within an xy plane in a two-dimensional triangular lattice. Black arrows: magnetic moment vectors. C_{3z}: threefold rotation along z. $\mathcal{PT}$: a combination of inversion symmetry $\mathcal{P}$ and time-reversal symmetry $\mathcal{T}$. $U\tau$: a combination of spinor symmetry U and translation τ. (b)(e) Counterclockwise (CCW) and clockwise (CW) spin chirality with out-of-plane polarization $\pm P_{\rm FE}^z$, respectively. ± 1: κ value. Orange shadow: magnetic unit cell. Blue star: inversion center connecting YAFM in (b) and (e). Blue circle: rotation axis of C_{3z}. (c), (f) Berry curvature $\Omega_n^z(\boldsymbol{k})$ in the first Brillouin zone. K' and M' denote $-K$ and $-M$. Darkness: magnitude of $\Omega_n^z(\boldsymbol{k})$. (d), (g) Spin-polarized bands along $-X$-Γ-X (X: a generic wave vector). Color of bands: magnitude of S_z polarization.

in weak-SOC NCAFs, a quasisymmetry framework lying between MSG and SSG is urgently needed. Triangular lattices, with simple geometry, abundant material candidates, and typical noncollinear magnetic ground states, serve as ideal platforms for exploring novel coupling effects and fundamental physical mechanisms in NCAFs.

In this work, based on symmetry analysis, Monte Carlo (MC) simulations, and first-principles calculations, we propose a unified quasisymmetry framework for two-dimensional triangular-lattice NCAFs with YAFM, exploring the coexistence, coupling, and manipulation of multiple physical properties in a weak SOC regime. The framework reveals physical phenomena beyond the conventional descriptions of MSG and SSG and establishes a design principle for multifunctional integration and reversible field control in NCAF-based spintronics. MC simulations demonstrate triangular lattices favor YAFM stabilized by competing interactions. Symmetry analysis in triangular-lattice YAFM reveals the robust coexistence and coupling of ferroelectric polarization, Berry curvature, and AFM-induced spin splitting, which remain invariant under arbitrary in-plane rotation of YAFM. YAFM with opposite spin chirality is interconnected by inversion operation, mediating the coupling among these physical properties. Crucially, chirality-ferroelectricity locking allows synergistic switching of spin chirality, Berry curvature, and AFM-induced spin splitting upon reversing the ferroelectric polarization, enabling nonvolatile electric-field manipulation. Further, spin canting breaks effective time-reversal symmetry, introducing SOC-free valley polarization and a net magnetic moment coupled to the above properties. Reorienting spin canting enforces transformations of these coupled properties under effective time-reversal operation. Diverse functionalities including magnetoelectric coupling, circular dichroic Hall effect (CDHE), nonrelativistic anisotropic Edelstein effect, and anomalous valley Hall effect (AVHE) can be realized with the coexistence of multiple coupled properties. High-throughput calculations on triangular-lattice MXenes identify monolayer $Zr_2VC_2X_2$ (X = F, Cl, Br, I) as promising candidates hosting YAFM ground states, with $Zr_2VC_2Cl_2$ exhibiting the highest Néel temperature. First-principles calculations confirm the integration of multiple coupled properties, their reversible tunability, and the resulting multifunctionality. This work bridges symmetry-guided design, material discovery, and tunable multifunctionality in noncollinear antiferromagnetic spintronics.

II. RESULTS AND DISCUSSION

A. Symmetry framework for triangular-lattice coplanar YAFM

The magnetic phase diagram (Fig. S1 [33]) obtained from MC simulations reveals YAFM, stabilized by competing nearest-neighbor AFM and next-nearest-neighbor FM interactions, emerges as a favored noncollinear ground state in two-dimensional triangular lattices, where spins in each of the three magnetic sublattices are aligned parallel but mutually rotated by 120°, as illustrated in Fig. 1(a).

As exemplified in Figs. 1(b) and 1(e), MSG symmetry analysis reveals that YAFM breaks inversion symmetry $\mathcal{P}$, enabling an out-of-plane electric polarization constrained by threefold rotation symmetry C_{3z}. Considering vector-spin chirality [34,35] $\kappa = \frac{2}{3\sqrt{3}}\sum_{\langle i,j\rangle}[\boldsymbol{S}_i \times \boldsymbol{S}_j]_z$, where $\boldsymbol{S}_{i,j}$ are nearest-neighbor spins, two opposite arrangements of spin chirality can be identified in YAFM, here marked as counterclockwise (CCW) and clockwise (CW) spin chirality, which are connected by an inversion operation. Consequently, electric polarization $\boldsymbol{P}$ transforms as $\boldsymbol{P}' = \mathcal{P}\boldsymbol{P} = -\boldsymbol{P}$ under inversion [36], leading to opposite polarizations in Figs. 1(b) and 1(e). That is, a chirality-polarization locking exists, with opposite chirality leading to opposite polarizations. Such a feature implies that the electric field can act as an inversion connector, tuning those spin-chirality-related properties and thus offering a promising route toward multifunctional integration and external-field control. Two properties of interest in collinear magnets, Berry curvature and spin splitting, are highlighted next as representative examples.

Berry curvature $\boldsymbol{\Omega}_n(\boldsymbol{k})$ satisfies $\boldsymbol{\Omega}_n(\boldsymbol{k}) = \boldsymbol{\Omega}_n(-\boldsymbol{k})$ under $\mathcal{P}$, $\boldsymbol{\Omega}_n(\boldsymbol{k}) = -\boldsymbol{\Omega}_n(-\boldsymbol{k})$ under time-reversal symmetry $\mathcal{T}$, and $\boldsymbol{\Omega}_n(\boldsymbol{k})$ transforms as an ordinary vector under rotation and remains invariant under translation τ, as revealed by MSG analysis [37,38]. Given YAFM violates the joint symmetry $\mathcal{PT}$, a nonzero $\boldsymbol{\Omega}_n(\boldsymbol{k})$ over the Brillouin zone is anticipated. C_{3z} in YAFM further constrains $\boldsymbol{\Omega}_n(\boldsymbol{k})$ to $\Omega_n^z(\boldsymbol{k})$ with threefold-rotation symmetry. Considering the weak SOC in a vast number of magnets, an additional effective time-reversal symmetry for $\Omega_n^z(\boldsymbol{k})$ arising from the coplanar spin arrangements as revealed via SSG symmetry analysis (Note S1 [33]) further enforces $\Omega_n^z(\boldsymbol{k}) = -\Omega_n^z(-\boldsymbol{k})$, as illustrated in Figs. 1(c) and 1(f). Moreover, the inversion operation connecting opposite spin chirality enforces $\Omega_n^{z'}(\boldsymbol{k}') = \mathcal{P}\Omega_n^z(\boldsymbol{k}) = \Omega_n^z(-\boldsymbol{k})$, mapping Berry curvature at $\boldsymbol{k}$ in one chirality to that at $-\boldsymbol{k}$ in the other [Figs. 1(c) and 1(f)].

Spin splitting in momentum space is also governed by underlying symmetry. YAFM inherently violates $\mathcal{PT}$ symmetry and $U\tau$ symmetry even in the nonrelativistic limit, satisfying the symmetry condition for nonrelativistic momentum-dependent spin splitting [39]. Therefore, an AFM-induced nonrelativistic spin splitting is expected. Similarly, in the weak SOC limit, an out-of-plane spin polarization satisfying effective time-reversal symmetry $\epsilon(\boldsymbol{k}, S_z) = \epsilon(-\boldsymbol{k}, -S_z)$ is allowed in the coplanar YAFM shown in Fig. 1, as revealed by SSG symmetry analysis (Note S2 [33]). By extending the definition of spin splitting in altermagnetism [27] as the energy splitting between opposite S_z components $\Delta\epsilon(\boldsymbol{k}, S_z) = \epsilon(\boldsymbol{k}, S_z) - \epsilon(\boldsymbol{k}, -S_z)$, an effective time-reversal symmetry for spin splitting $\Delta\epsilon(\boldsymbol{k}, S_z) = -\Delta\epsilon(-\boldsymbol{k}, S_z)$ is revealed (Note S2 [33]), as shown in Figs. 1(d) and 1(g). It transforms with spin chirality as $\Delta\epsilon'(\boldsymbol{k}', S_z') = \mathcal{P}\Delta\epsilon(\boldsymbol{k}, S_z) = \Delta\epsilon(-\boldsymbol{k}, S_z)$, establishing a correspondence between the spin splitting at $\boldsymbol{k}$ and $-\boldsymbol{k}$ in opposite chirality [Figs. 1(d) and 1(g)]. As such, the inversion-induced spin-chirality transformation mediates the coupling among spin chirality, ferroelectricity, Berry curvature, and spin splitting. Owing to chirality-ferroelectricity locking, the electric-field-controlled reversal of polarization triggers the switching of Berry curvature, spin splitting, and spin chirality. This unified quasisymmetry framework effectively captures the physical reality of triangular-lattice YAFM with weak SOC, unveiling the coexistence, coupling, and manipulation of multiple physical properties. Distinct from the MSG description, the above analyses of $\boldsymbol{P}$, $\Omega_n^z(\boldsymbol{k})$, and spin splitting with spin chirality remain invariant regardless of the in-plane rotation of YAFM, and their coexistence lies beyond the SSG description, thereby the quasisymmetry framework is established as complementary to MSG and SSG. Various degrees of freedom can be predicted with such a symmetry-guided framework.

B. Electric-switchable coupled properties in $Zr_2VC_2Cl_2$

Subsequently, high-throughput calculations were employed to identify dynamically stable semiconductors with YAFM ground states [Fig. 2(a)]. Double transition metal

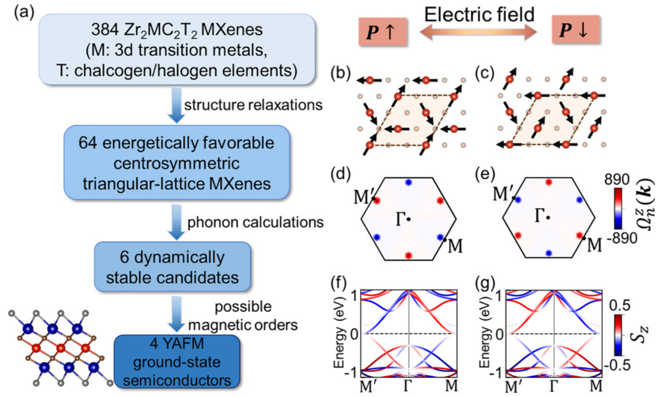

FIG. 2. Material screening and realization of electric-field-controlled coupled properties. (a) Screening scheme for centrosymmetric triangular-lattice MXenes hosting YAFM ground states. Inset: side view of YAFM ground-state candidates $Zr_2VC_2X_2$, with Zr (blue), V (red), C (brown), and X (gray). (b), (c) Top views of $Zr_2VC_2Cl_2$ with YAFM, showing only V and C atoms for clarity, (d), (e) Berry curvatures in the first Brillouin zone, and (f), (g) S_z-resolved bands along ΓM and its time-reversal path $\Gamma M'$, under opposite polarization states, $\boldsymbol{P}\uparrow$ and $\boldsymbol{P}\downarrow$. M' denotes $-M$. The Fermi level is set to zero.

MXenes with triangular lattices were selected for screening due to their chemical diversity and well-established synthesis methods [40]. Focusing on zirconium-containing carbides for their exceptional thermal stability and two-dimensional nature [41], we identified monolayer $Zr_2VC_2X_2$ (X = F, Cl, Br, I) as promising YAFM candidates, with $Zr_2VC_2Cl_2$ exhibiting the highest estimated Néel temperature T_N of ∼190 K among them (Figs. S2–S6 [33]). Magnetic anisotropy energy calculations exemplified by $Zr_2VC_2Cl_2$ reveal an easy xy plane and show a negligible energy variation for YAFM rotation within an xy plane (Fig. S5 [33]).

Below we choose the in-plane YAFM with opposite spin chirality [Figs. 2(b) and 2(c)] to demonstrate the electric polarization, Berry curvature, and spin splitting properties in $Zr_2VC_2Cl_2$. For electric polarization $\boldsymbol{P}$, first-principles calculations yield $P_z = 1.73 \times 10^{-7}$ μC/m while $P_{x,y}$ approach zero, and exhibit a sign reversal of P_z upon spin chirality reversal, as represented by $\boldsymbol{P}\uparrow$ and $\boldsymbol{P}\downarrow$ in Fig. 2. A strong magnetoelectric coupling effect, with the coupling strength on the order of 10^{-3} eÅ based on the generalized spin current model [42], the spin-electronic magnetoelectric constant of $\alpha_{zz} = 12.3$ ps/m, and the spin-texture-dependent polarizations revealed by first-principles calculations, is obtained in $Zr_2VC_2Cl_2$ (Figs. S7–S9 [33]). These results confirm the predicted chirality-polarization locking, indicating both spin chirality and polarization could be controlled by magnetic and electric fields. For the modulation of $\boldsymbol{P}$, it could be controlled by applying a magnetic field that changes the spin configuration, as demonstrated experimentally in $TbMnO_3$ [43] and $MnAu_2$ [44]. For the reversal of spin chirality, applying an electric field lifts the degeneracy between (CCW, $\boldsymbol{P}\uparrow$) and (CW, $\boldsymbol{P}\downarrow$) states, favoring the spin chirality with $\boldsymbol{P}$ oriented along the field. A realistic transition path for spin-chirality reversal is proposed, involving spin rotation around x with an energy barrier of ∼77 μeV/f.u. The combination of such a low switching barrier, sizable polarization, and strong magnetoelectric coupling in $Zr_2VC_2Cl_2$ enables the efficient and practical electric-field control of spin chirality and its coupled $\boldsymbol{P}$, requiring an electric field of about 0.1 V/Å (Fig. S10 [33]).

The calculated Berry curvatures in Figs. 2(d) and 2(e) exhibit $\Omega_n^z(\boldsymbol{k})$ with threefold rotation symmetry and effective time-reversal symmetry in the weak-SOC $Zr_2VC_2Cl_2$ with coplanar YAFM [See also $\Omega_n^z(\boldsymbol{k})$ without SOC in Fig. S11 [33]], as predicted by the above symmetry analysis. Combined with the transformation $\Omega_n^{z'}(\boldsymbol{k}') = \Omega_n^z(-\boldsymbol{k})$, a reversal of Berry curvature between opposite spin chirality is demonstrated in Figs. 2(d) and 2(e). As shown in Figs. 2(f) and 2(g), first-principles calculations reveal spontaneous antisymmetric spin splitting [$\Delta\epsilon(\boldsymbol{k}, S_z) = -\Delta\epsilon(-\boldsymbol{k}, S_z)$]. Singlet states [18,45,46] without symmetry-imposed spin degeneracy of the S_z component at each wave vector along ΓM and $\Gamma M'$ are unveiled by MSG and SSG analysis, thus allowing finite S_z polarization. The opposite S_z polarizations and opposite spin splitting along ΓM and $\Gamma M'$ in weak-SOC $Zr_2VC_2Cl_2$ with coplanar YAFM satisfy the effective time-reversal symmetry, consistent with our symmetry analysis (see also antisymmetric spin splitting without SOC in Fig. S11 [33]). The combination of $\Delta\epsilon(\boldsymbol{k}, S_z) = -\Delta\epsilon(-\boldsymbol{k}, S_z)$ and $\Delta\epsilon'(\boldsymbol{k}', S_z') = \Delta\epsilon(-\boldsymbol{k}, S_z)$ leads to opposite spin splitting between opposite spin chirality [$\Delta\epsilon(\boldsymbol{k}, S_z) = -\Delta\epsilon'(\boldsymbol{k}', S_z')$, Figs. 2(f) and 2(g)], demonstrating spin chirality locking with spin splitting. These results validate the quasisymmetry framework, demonstrating coupled chirality, $\boldsymbol{P}$, $\Omega_n^z(\boldsymbol{k})$, and spin splitting, as well as realistic electric-field switching of these properties in a nonvolatile and reversible fashion through the bridge of $\boldsymbol{P}$.

C. Field-tunable multifunctionality in coplanar YAFM

Considering the opposite $\Omega_n^z(\boldsymbol{k})$ at time-reversal-related valleys in weak-SOC coplanar YAFM, valley-contrasted optical circular dichroism arises [47]. Irradiating right-handed circularly polarized light (δ_-) excites carriers with $-\Omega_n^z(\boldsymbol{k})$ and induces a transverse Hall voltage U, while irradiating left-handed circularly polarized light (δ_+) excites carriers with $\Omega_n^z(\boldsymbol{k})$ and induces an opposite U, realizing CDHE. Combining the directions of $\boldsymbol{P}$ and U, four states shown in Fig. 3(a) are obtained, $\boldsymbol{P}\!\uparrow U-$, $\boldsymbol{P}\!\uparrow U+$, $\boldsymbol{P}\!\downarrow U-$, and $\boldsymbol{P}\!\downarrow U+$. Counterclockwise chirality with δ_+ introduces $\boldsymbol{P}\!\uparrow U+$, and out-of-plane electric field E_z reverses $\boldsymbol{P}$ to $\boldsymbol{P}\!\downarrow U+$. Alternatively, changing the light polarization induces $\boldsymbol{P}\!\uparrow U-$, and subsequent E_z switches it to $\boldsymbol{P}\!\downarrow U-$. Such multistate control is validated in $Zr_2VC_2Cl_2$, where the degree of circular polarization [47] $\eta(\boldsymbol{k})$ reaches ±100% around M and M' for both $\boldsymbol{P}\!\uparrow$ and $\boldsymbol{P}\!\downarrow$ states [Fig. 3(b)], demonstrating fully selective absorption by circularly polarized light.

Additionally, a spin-polarized current can be generated owing to the AFM-induced antisymmetric spin splitting. This further enhances multifunctionality and enriches tuning knobs. As shown in the left panel of Fig. 3(c), under a negative electric gating (or hole doping), applying an electric field $\boldsymbol{E}$ along $+y$ can induce a nonequilibrium redistribution of holes from the lower side to the upper side of the Fermi surface, yielding an accumulation of holes with $+S_z$. Reversing $\boldsymbol{E}$ to $-y$ or reversing $\boldsymbol{P}$ via E_z [right panel of Fig. 3(c)] yields an accumulation of holes with $-S_z$. No net

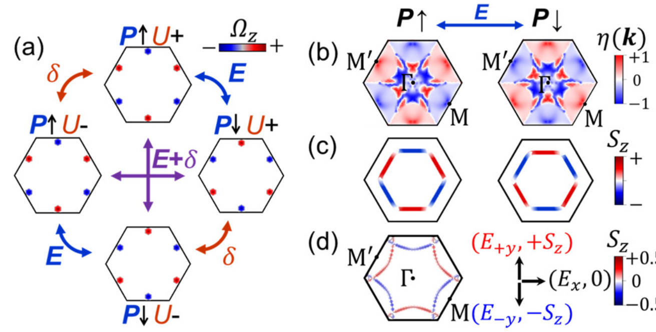

FIG. 3. Multifunctionality and multistate control enabled by coplanar YAFM and their realization in $Zr_2VC_2Cl_2$. (a) Schematics of multistate transformation under electric field $\boldsymbol{E}$ and circularly polarized light irradiation δ. The color map denotes the value of Berry curvatures at valleys for the valence band. (b) Degrees of circular polarization in $Zr_2VC_2Cl_2$ for $\boldsymbol{P}\!\uparrow$ and $\boldsymbol{P}\!\downarrow$ states, respectively. (c) Schematics of S_z-resolved constant-energy contour at $\mu < 0$ in coplanar YAFM exhibiting $\boldsymbol{P}\!\uparrow$ and $\boldsymbol{P}\!\downarrow$, respectively. μ: chemical potential relative to Fermi energy. (d) Spin-resolved constant-energy contour at $\mu = -0.18$ eV in $Zr_2VC_2Cl_2$. Hexagons represent the first Brillouin zone, and M' denotes $-M$.

accumulation of carriers with S_z arises under in-plane $\boldsymbol{E}$ along $\pm x$. These suggest an anisotropic Edelstein effect. Notably, unlike conventional SOC-induced spin-polarized currents, the spin-polarized currents proposed here originate from AFM order, avoiding the need for heavy elements with strong SOC. Moreover, the AFM origin allows magnetic-field control of such an Edelstein effect, and electric-field tunability considering the coupling among spin chirality, ferroelectricity, and spin splitting. The spin-resolved constant-energy contour at $\mu = -0.18$ eV in $Zr_2VC_2Cl_2$ validates the realization of field-tunable anisotropic Edelstein effects [Fig. 3(d)].

D. Field-tunable multifunctionality in noncoplanar YAFM

Moreover, a magnetic field $\boldsymbol{H}$ along z induces a noncoplanar YAFM with spins canted out of plane by an angle ω [see insets in Figs. 4(a)–4(d)]. This breaks the effective time-reversal symmetry and introduces additional degrees of freedom, valley polarization $\Delta_{c/v}$, and net magnetic moment $\boldsymbol{M}_{\uparrow/\downarrow}$, which couple to spin chirality (CCW/CW), ferroelectric polarization $\boldsymbol{P}_{\uparrow/\downarrow}$, Berry curvature $\Omega_n^z(\boldsymbol{k})$, and spin splitting $\Delta\epsilon(\boldsymbol{k}, S_z)$. The external-field manipulation of these coupled properties is depicted in Figs. 4(a)–4(d) and their transformations are summarized in Table I. Applying an out-of-plane electric field $\boldsymbol{E}$ switches [CCW, $\boldsymbol{P}_\uparrow$, $\Delta\epsilon(\boldsymbol{k}, S_z)$, $\Omega_n^z(\boldsymbol{k})$, $\Delta_{c/v}$, $\boldsymbol{M}_\uparrow$] in Fig. 4(a) to [CW, $\boldsymbol{P}'_\downarrow$, $\Delta\epsilon'(-\boldsymbol{k}', S_z')$, $\Omega_n^{z'}(-\boldsymbol{k}')$, $-\Delta'_{c/v}$, $\boldsymbol{M}'_\uparrow$] in Fig. 4(b) via inversion-induced spin chirality transformation. In contrast, a magnetic field $\boldsymbol{H}$ switches it to [CCW, $\boldsymbol{P}'_\uparrow$, $-\Delta\epsilon'(-\boldsymbol{k}', S_z')$, $-\Omega_n^{z'}(-\boldsymbol{k}')$, $-\Delta'_{c/v}$, $\boldsymbol{M}'_\downarrow$] in Fig. 4(c) via effective time-reversal-induced spin canting reorientation. For CCW YAFM with $\omega = 25^\circ$ [Fig. 4(a)], the valley polarizations in $Zr_2VC_2Cl_2$ reach $\Delta_c = 8$ meV and $\Delta_v = 10$ meV, both larger than $FeCl_2$ (5 meV) [48] and WSe_2/CrI_3 heterostructures (0.3–1 meV) [49,50]. The calculated anomalous valley Hall conductivity σ_{xy} reaches a maximum of ~130 S/cm, underscoring a pronounced AVHE

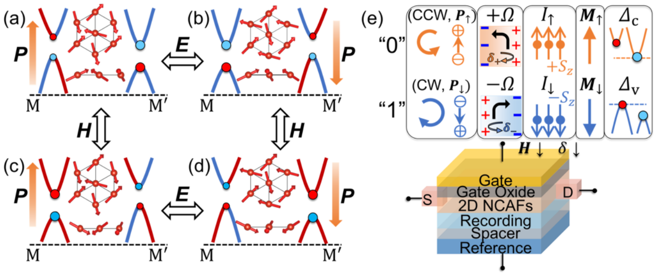

FIG. 4. Coexistence, coupling, and manipulation of diverse physical properties generally realized in noncoplanar YAFM and the prototype spintronic device. (a)–(d) Schematic of electric-field ($\boldsymbol{E}$) and magnetic-field ($\boldsymbol{H}$) control of coupled properties, including spin chirality (CCW/CW), ferroelectric polarization ($\boldsymbol{P}_{\uparrow/\downarrow}$, $\boldsymbol{P}$ along $\pm z$), Berry curvature [$\Omega_n^z(\boldsymbol{k})$], spin splitting [$\Delta\epsilon(\boldsymbol{k}, S_z)$], magnetic moment ($\boldsymbol{M}_{\uparrow/\downarrow}$, a net magnetic moment along $\pm z$), and valley polarization ($\Delta_{c/v}$, energy difference between valleys in conduction or valence band). M' denotes $-M$. Orange arrow: $\boldsymbol{P}$ along $\pm z$. Red (blue) curve: bands with positive (negative) S_z polarization. Red (blue) solid circles denote positive (negative) $\Omega_n^z(\boldsymbol{k})$ and the circle size represents its magnitude. (e) Schematic of a field-effect transistor based on two-dimensional NCAFs and attached with a magnetic tunnel junction. S, D: source, drain.

response in $Zr_2VC_2Cl_2$ (Fig. S12 [33]). Notably, the mechanism of valley polarization here differs from the conventional one in collinear magnets which requires both SOC and intrinsic exchange interactions [51,52]. Instead, SOC is not necessary for valley polarization emerging in this case, and the breaking of effective time-reversal symmetry is actually the essential factor.

As schematized in Fig. 4(e), the external-field manipulation of six coupled degrees of freedom, including spin chirality, $\boldsymbol{P}$, $\boldsymbol{\Omega}$, spin splitting, $\boldsymbol{M}$, and valley polarization, can generate 48 states ($2 \times 2 \times 3 \times 2 \times 2$), suggesting a significant potential for constructing advanced devices based on NCAFs. $\boldsymbol{P}$ and chirality can be switched by an out-of-plane $\boldsymbol{E}$ and identified through dielectricity or second-harmonic generation measurements [43,53–55]. Valley-contrasting $\boldsymbol{\Omega}$ can be distinguished through CDHE [56]. Nonrelativistic anisotropic spin-polarized currents $I_{\uparrow/\downarrow}$, featuring $\pm S_z$ carrier accumulation, can be generated by applying a gate voltage and an in-plane $\boldsymbol{E}$ along different directions, such as $+y$, $-y$, or parallel to x. Such Edelstein effects can be detected through tunneling magnetoresistance using a magnetic tunnel junction with an efficient read-write separated path [Fig. 4(e)] [57,58]. $\boldsymbol{M}$ can be modulated by $\boldsymbol{H}$ along z and tested by the Hall effect or magneto-optical Kerr effect [59]. For valley polarization $\Delta_{c/v}$, different Berry curvatures in the valleys induce distinct transverse Hall voltages, resulting in AVHE under in-plane $\boldsymbol{E}$ and specific gate voltage, with optional magnetic field involvement. Therefore, the external-field tunability, flexible cross-degree-of-freedom manipulation, and multifunctional integration are achieved in two-dimensional noncollinear antiferromagnets, enabling devices adaptable to different application requirements.

TABLE I. Transformations under symmetry operations in two-dimensional triangular lattices. The notations of operations follow the convention of Ref. [26]. $\boldsymbol{k}$, κ, S_z, P_z, Ω_n^z, $\Delta\epsilon$, $\Delta_{c/v}$, M_z, and I denote, respectively, the vector-spin chirality, wave vector, z component of the spin vector, electric polarization and Berry curvature, the energy splitting between opposite S_z polarization, valley polarization in a conduction or valence band, z component of the magnetic moment, and the S_z-polarized current. "+" ("−") refers to the sign preservation (reversal) of a physical quantity under an operation.

	$\boldsymbol{k}$	S_z	κ	P_z	Ω_n^z	$\Delta\epsilon$	$\Delta_{c/v}$	M_z	I
$\{1\|-1\|(0,0,0)\}$	−	+	−	−	+	+	−	+	−
$\{m_{001}\|1\|(0,0,0)\}$	−	−	+	+	−	−	−	−	+

III. CONCLUSION

In conclusion, through symmetry analysis, we unveiled the coexistence, coupling, and manipulation of multiple physical properties in two-dimensional triangular-lattice YAFM, including AFM-induced spin splitting, SOC-free valley polarization, spin chirality driven ferroelectricity, and Berry curvature, extending the descriptions of MSG and SSG. The spin chirality transformation mediates the coupling among these properties, enabling their synergistic switching. Chirality-ferroelectricity locking reveals reversible manipulation of these properties via electric and magnetic fields. Multiple functionalities, including magnetoelectric coupling, CDHE, nonrelativistic anisotropic Edelstein effect, and AVHE, are enabled with these coupled properties. Among monolayer MXenes $Zr_2VC_2X_2$ (X = F, Cl, Br, I) hosting YAFM ground states, first-principles calculations, exemplified by $Zr_2VC_2Cl_2$ with the highest Néel temperature, confirmed the symmetry-predicted multiple coupled properties, external-field manipulation, and multifunctionality. Based on these findings, we designed a prototype spintronic device with field-tunable multifunctional integration, where the spin chirality, ferroelectricity, CDHE, Edelstein effect, and AVHE can be regulated by ferroelectric polarization reversal via an electric field and spin-configuration transformation via a magnetic field. This work provides a unified quasisymmetry framework that enables multifunctionality and cross-degree-of-freedom manipulation in weak-SOC NCAFs, facilitating the development of next-generation NCAF-based devices.

ACKNOWLEDGMENTS

This work is supported by funds from the National Key Research and Development Program of China (Grants No. 2022YFA1204100, No. 2024YFA1207803, No. 2021YFA1201501) and the National Natural Science Foundation of China (Grants No. 62488201 and No. 52272172).

DATA AVAILABILITY

The data that support the findings of this article are not publicly available. The data are available from the authors upon reasonable request.

[1] J. Han, R. Cheng, L. Liu, H. Ohno, and S. Fukami, Coherent antiferromagnetic spintronics, Nat. Mater. **22**, 684 (2023).
[2] L. Bai, W. Feng, S. Liu, L. Šmejkal, Y. Mokrousov, and Y. Yao, Altermagnetism: Exploring new frontiers in magnetism and spintronics, Adv. Funct. Mater. **34**, 2409327 (2024).
[3] B. H. Rimmler, B. Pal, and S. S. P. Parkin, Non-collinear antiferromagnetic spintronics, Nat. Rev. Mater. **10**, 109 (2025).
[4] H. Chen, Q. Niu, and A. H. MacDonald, Anomalous Hall effect arising from noncollinear antiferromagnetism, Phys. Rev. Lett. **112**, 017205 (2014).
[5] J. Kübler and C. Felser, Non-collinear antiferromagnets and the anomalous Hall effect, Europhys. Lett. **108**, 67001 (2014).
[6] S. Nakatsuji, N. Kiyohara, and T. Higo, Large anomalous Hall effect in a non-collinear antiferromagnet at room temperature, Nature (London) **527**, 212 (2015).
[7] A. K. Nayak, J. E. Fischer, Y. Sun, B. Yan, J. Karel, A. C. Komarek, C. Shekhar, N. Kumar, W. Schnelle, J. Kübler, *et al.*, Large anomalous Hall effect driven by a nonvanishing Berry curvature in the noncolinear antiferromagnet Mn_3Ge, Sci. Adv. **2**, e1501870 (2016).
[8] H. Tsai, T. Higo, K. Kondou, T. Nomoto, A. Sakai, A. Kobayashi, T. Nakano, K. Yakushiji, R. Arita, S. Miwa, *et al.*, Electrical manipulation of a topological antiferromagnetic state, Nature (London) **580**, 608 (2020).
[9] V. Baltz, A. Manchon, M. Tsoi, T. Moriyama, T. Ono, and Y. Tserkovnyak, Antiferromagnetic spintronics, Rev. Mod. Phys. **90**, 015005 (2018).
[10] H. Chen, L. Liu, X. Zhou, Z. Meng, X. Wang, Z. Duan, G. Zhao, H. Yan, P. Qin, and Z. Liu, Emerging antiferromagnets for spintronics, Adv. Mater. **36**, 2310379 (2024).
[11] J. Železný, Y. Zhang, C. Felser, and B. Yan, Spin-polarized current in noncollinear antiferromagnets, Phys. Rev. Lett. **119**, 187204 (2017).
[12] J. Hwang, E. S. Choi, F. Ye, C. R. Dela Cruz, Y. Xin, H. D. Zhou, and P. Schlottmann, Successive magnetic phase transitions and multiferroicity in the spin-one triangular-lattice antiferromagnet $Ba_3NiNb_2O_9$, Phys. Rev. Lett. **109**, 257205 (2012).
[13] C. Liu, W. Ren, and S. Picozzi, Spin-chirality-driven multiferroicity in van der Waals monolayers, Phys. Rev. Lett. **132**, 086802 (2024).
[14] H. Mitamura, R. Watanuki, K. Kaneko, N. Onozaki, Y. Amou, S. Kittaka, R. Kobayashi, Y. Shimura, I. Yamamoto, K. Suzuki, *et al.*, Spin-chirality-driven ferroelectricity on a perfect triangular lattice antiferromagnet, Phys. Rev. Lett. **113**, 147202 (2014).
[15] Y. Tokura and S. Seki, Multiferroics with spiral spin orders, Adv. Mater. **22**, 1554 (2010).
[16] J.-J. Zhang, L. Lin, Y. Zhang, M. Wu, B. I. Yakobson, and S. Dong, Type-II multiferroic $Hf_2VC_2F_2$ MXene monolayer with high transition temperature, J. Am. Chem. Soc. **140**, 9768 (2018).
[17] X. Yang, A. Guo, J. Yang, J. Chen, K. Meng, S. Hu, R. Duan, M. Zhu, W. Shi, Y. Qin, *et al.*, Halogenated-edge polymeric semiconductor for efficient spin transport, Nat. Commun. **15**, 8368 (2024).
[18] L. Elcoro, B. J. Wieder, Z. Song, Y. Xu, B. Bradlyn, and B. A. Bernevig, Magnetic topological quantum chemistry, Nat. Commun. **12**, 5965 (2021).
[19] A. Manchon, H. C. Koo, J. Nitta, S. M. Frolov, and R. A. Duine, New perspectives for Rashba spin–orbit coupling, Nat. Mater. **14**, 871 (2015).
[20] N. Nagaosa, J. Sinova, S. Onoda, A. H. MacDonald, and N. P. Ong, Anomalous Hall effect, Rev. Mod. Phys. **82**, 1539 (2010).
[21] J. Sinova, S. O. Valenzuela, J. Wunderlich, C. H. Back, and T. Jungwirth, Spin Hall effects, Rev. Mod. Phys. **87**, 1213 (2015).
[22] H. Watanabe, H. C. Po, and A. Vishwanath, Structure and topology of band structures in the 1651 magnetic space groups, Sci. Adv. **4**, eaat8685 (2018).
[23] R. Yu, W. Zhang, H.-J. Zhang, S.-C. Zhang, X. Dai, and Z. Fang, Quantized anomalous Hall effect in magnetic topological insulators, Science **329**, 61 (2010).
[24] W. Brinkman and R. J. Elliott, Space group theory for spin waves, J. Appl. Phys. **37**, 1457 (1966).
[25] W. F. Brinkman, R. J. Elliott, and R. E. Peierls, Theory of spin-space groups, Proc. R. Soc. Lond. A **294**, 343 (1966).
[26] X. Chen, J. Ren, Y. Zhu, Y. Yu, A. Zhang, P. Liu, J. Li, Y. Liu, C. Li, and Q. Liu, Enumeration and representation theory of spin space groups, Phys. Rev. X **14**, 031038 (2024).
[27] M. Gu, Y. Liu, H. Zhu, K. Yananose, X. Chen, Y. Hu, A. Stroppa, and Q. Liu, Ferroelectric switchable altermagnetism, Phys. Rev. Lett. **134**, 106802 (2025).
[28] D. Litvin, Spin point groups, Acta Cryst. A **33**, 279 (1977).
[29] D. B. Litvin and W. Opechowski, Spin groups, Physica **76**, 538 (1974).
[30] P. Liu, J. Li, J. Han, X. Wan, and Q. Liu, Spin-group symmetry in magnetic materials with negligible spin-orbit coupling, Phys. Rev. X **12**, 021016 (2022).
[31] L. Šmejkal, J. Sinova, and T. Jungwirth, Beyond conventional ferromagnetism and antiferromagnetism: A phase with nonrelativistic spin and crystal rotation symmetry, Phys. Rev. X **12**, 031042 (2022).
[32] L. Šmejkal, J. Sinova, and T. Jungwirth, Emerging research landscape of altermagnetism, Phys. Rev. X **12**, 040501 (2022).
[33] See Supplemental Material at http://link.aps.org/supplemental/10.1103/x52d-htvb for computational methods; notes regarding effective time-reversal symmetry for Berry curvature, S_z polarization, and spin splitting $\Delta\epsilon(\boldsymbol{k}, S_z)$; magnetic ground-state phase diagram of two-dimensional centrosymmetric triangular lattices obtained by MC simulations; stable configurations, phonon dispersions, first-principles-calculated magnetic ground configurations, magnetic coefficients, MC-simulated YAFM ground states, and Néel temperatures of $Zr_2VC_2X_2$; spin-spiral calculation and magnetic anisotropy energy of $Zr_2VC_2Cl_2$; magnetoelectric coupling effect in $Zr_2VC_2Cl_2$; electric field switching of spin chirality and ferroelectric polarization in $Zr_2VC_2Cl_2$; Berry curvatures and spin splitting without SOC for $Zr_2VC_2Cl_2$ showing opposite polarizations; and energy-dependent anomalous Hall conductivity for $Zr_2VC_2Cl_2$ with noncoplanar spin configurations, which includes Refs. [16,26,38,42,45,60–88].
[34] D. Grohol, K. Matan, J.-H. Cho, S.-H. Lee, J. W. Lynn, D. G. Nocera, and Y. S. Lee, Spin chirality on a two-dimensional frustrated lattice, Nat. Mater. **4**, 323 (2005).
[35] T. Inami, M. Nishiyama, S. Maegawa, and Y. Oka, Magnetic structure of the kagome lattice antiferromagnet potassium jarosite $KFe_3(OH)_6(SO_4)_2$, Phys. Rev. B **61**, 12181 (2000).

[36] Y. Zhu, J.-T. Sun, J. Pan, J. Deng, and S. Du, Enforced symmetry breaking for anomalous valley Hall effect in two-dimensional hexagonal lattices, Phys. Rev. Lett. **134**, 046403 (2025).

[37] M. T. Suzuki, T. Koretsune, M. Ochi, and R. Arita, Cluster multipole theory for anomalous Hall effect in antiferromagnets, Phys. Rev. B **95**, 094406 (2017).

[38] D. Xiao, M.-C. Chang, and Q. Niu, Berry phase effects on electronic properties, Rev. Mod. Phys. **82**, 1959 (2010).

[39] L.-D. Yuan, Z. Wang, J.-W. Luo, and A. Zunger, Prediction of low-Z collinear and noncollinear antiferromagnetic compounds having momentum-dependent spin splitting even without spin-orbit coupling, Phys. Rev. Mater. **5**, 014409 (2021).

[40] M. Naguib, M. W. Barsoum, and Y. Gogotsi, Ten years of progress in the synthesis and development of MXenes, Adv. Mater. **33**, 2103393 (2021).

[41] J. Zhou, X. Zha, F. Y. Chen, Q. Ye, P. Eklund, S. Du, and Q. Huang, A two-dimensional zirconium carbide by selective etching of Al_3C_3 from nanolaminated $Zr_3Al_3C_5$, Angew. Chem. Int. Ed. Engl. **55**, 5008 (2016).

[42] H. J. Xiang, E. J. Kan, Y. Zhang, M. H. Whangbo, and X. G. Gong, General theory for the ferroelectric polarization induced by spin-spiral order, Phys. Rev. Lett. **107**, 157202 (2011).

[43] T. Kimura, T. Goto, H. Shintani, K. Ishizaka, T. Arima, and Y. Tokura, Magnetic control of ferroelectric polarization, Nature (London) **426**, 55 (2003).

[44] H. Masuda, T. Seki, J.-i. Ohe, Y. Nii, H. Masuda, K. Takanashi, and Y. Onose, Room temperature chirality switching and detection in a helimagnetic $MnAu_2$ thin film, Nat. Commun. **15**, 1999 (2024).

[45] Z. Song, A. Z. Yang, Y. Jiang, Z. Fang, J. Yang, C. Fang, H. Weng, and Z.-X. Liu, Constructions and applications of irreducible representations of spin-space groups, Phys. Rev. B **111**, 134407 (2025).

[46] Y. Xu, L. Elcoro, Z.-D. Song, B. J. Wieder, M. G. Vergniory, N. Regnault, Y. Chen, C. Felser, and B. A. Bernevig, High-throughput calculations of magnetic topological materials, Nature (London) **586**, 702 (2020).

[47] W. Yao, D. Xiao, and Q. Niu, Valley-dependent optoelectronics from inversion symmetry breaking, Phys. Rev. B **77**, 235406 (2008).

[48] T. Zhang, X. Xu, B. Huang, Y. Dai, and Y. Ma, 2D spontaneous valley polarization from inversion symmetric single-layer lattices, npj Comput. Mater. **8**, 64 (2022).

[49] K. L. Seyler, D. Zhong, B. Huang, X. Linpeng, N. P. Wilson, T. Taniguchi, K. Watanabe, W. Yao, D. Xiao, M. A. McGuire, *et al.*, Valley manipulation by optically tuning the magnetic proximity effect in WSe_2/CrI_3 heterostructures, Nano Lett. **18**, 3823 (2018).

[50] Z. Zhang, X. Ni, H. Huang, L. Hu, and F. Liu, Valley splitting in the van der Waals heterostructure WSe_2/CrI_3: The role of atom superposition, Phys. Rev. B **99**, 115441 (2019).

[51] X. Li, T. Cao, Q. Niu, J. Shi, and J. Feng, Coupling the valley degree of freedom to antiferromagnetic order, Proc. Natl. Acad. Sci. USA **110**, 3738 (2013).

[52] J. Qi, X. Li, Q. Niu, and J. Feng, Giant and tunable valley degeneracy splitting in $MoTe_2$, Phys. Rev. B **92**, 121403(R) (2015).

[53] M. Fiebig, V. V. Pavlov, and R. V. Pisarev, Second-harmonic generation as a tool for studying electronic and magnetic structures of crystals: Review, J. Opt. Soc. Am. B **22**, 96 (2005).

[54] E. D. Mishina, N. E. Sherstyuk, D. R. Barskiy, A. S. Sigov, Y. I. Golovko, V. M. Mukhorotov, M. De Santo, and T. Rasing, Domain orientation in ultrathin (Ba, Sr)TiO_3 films measured by optical second harmonic generation, J. Appl. Phys. **93**, 6216 (2003).

[55] E. Mishina, K. Grishunin, V. Bilyk, N. Sherstyuk, A. Sigov, V. Mukhortov, A. Ovchinnikov, and A. Kimel, Polarization switching in ferroelectric thin film induced by a single-period terahertz pulse, MRS Adv. **3**, 1901 (2018).

[56] K. F. Mak, K. L. McGill, J. Park, and P. L. McEuen, The valley Hall effect in MoS_2 transistors, Science **344**, 1489 (2014).

[57] T. Miyazaki and N. Tezuka, Giant magnetic tunneling effect in $Fe/Al_2O_3/Fe$ junction, J. Magn. Magn. Mater. **139**, L231 (1995).

[58] J. Sinova and T. Jungwirth, Surprises from the spin Hall effect, Phys. Today **70**(7), 38 (2017).

[59] B. Huang, G. Clark, E. Navarro-Moratalla, D. R. Klein, R. Cheng, K. L. Seyler, D. Zhong, E. Schmidgall, M. A. McGuire, D. H. Cobden, *et al.*, Layer-dependent ferromagnetism in a van der Waals crystal down to the monolayer limit, Nature (London) **546**, 270 (2017).

[60] G. Kresse and J. Furthmüller, Efficient iterative schemes for *ab initio* total-energy calculations using a plane-wave basis set, Phys. Rev. B **54**, 11169 (1996).

[61] G. Kresse and D. Joubert, From ultrasoft pseudopotentials to the projector augmented-wave method, Phys. Rev. B **59**, 1758 (1999).

[62] J. P. Perdew, K. Burke, and M. Ernzerhof, Generalized gradient approximation made simple, Phys. Rev. Lett. **77**, 3865 (1996); Erratum: **78**, 1396 (1997).

[63] S. L. Dudarev, G. A. Botton, S. Y. Savrasov, C. J. Humphreys, and A. P. Sutton, Electron-energy-loss spectra and the structural stability of nickel oxide: An LSDA+U study, Phys. Rev. B **57**, 1505 (1998).

[64] L. Wang, T. Maxisch, and G. Ceder, Oxidation energies of transition metal oxides within the GGA + U framework, Phys. Rev. B **73**, 195107 (2006).

[65] M. Kan, B. Wang, Y. H. Lee, and Q. Sun, A density functional theory study of the tunable structure, magnetism and metal-insulator phase transition in VS_2 monolayers induced by in-plane biaxial strain, Nano Res. **8**, 1348 (2015).

[66] H. He, H. Gao, W. Wu, S. Cao, J. Hong, D. Yu, G. Deng, Y. Gao, P. Zhang, H. Luo, *et al.*, Phonon instability and pressure-induced isostructural semiconductor-semimetal transition of monoclinic VO_2, Phys. Rev. B **94**, 205127 (2016).

[67] X. Gonze and C. Lee, Dynamical matrices, Born effective charges, dielectric permittivity tensors, and interatomic force constants from density-functional perturbation theory, Phys. Rev. B **55**, 10355 (1997).

[68] A. Togo and I. Tanaka, First principles phonon calculations in materials science, Scr. Mater. **108**, 1 (2015).

[69] R. D. King-Smith and D. Vanderbilt, Theory of polarization of crystalline solids, Phys. Rev. B **47**, 1651 (1993).

[70] R. Resta, M. Posternak, and A. Baldereschi, Towards a quantum theory of polarization in ferroelectrics: The case of $KNbO_3$, Phys. Rev. Lett. **70**, 1010 (1993).

[71] S.-W. Kim, H.-J. Kim, S. Cheon, and T.-H. Kim, Circular dichroism of emergent chiral stacking orders in quasi-one-dimensional charge density waves, Phys. Rev. Lett. **128**, 046401 (2022).

[72] H.-J. Kim, VASPBERRY: Berry curvature calculation code for VASP output (V1.0), Zenodo, 2018, doi:10.5281/zenodo.1402593.

[73] G. Pizzi, V. Vitale, R. Arita, S. Blügel, F. Freimuth, G. Géranton, M. Gibertini, D. Gresch, C. Johnson, T. Koretsune, *et al.*, Wannier90 as a community code: New features and applications, J. Phys.: Condens. Matter **32**, 165902 (2020).

[74] Q. Wu, S. Zhang, H.-F. Song, M. Troyer, and A. A. Soluyanov, WannierTools: An open-source software package for novel topological materials, Comput. Phys. Commun. **224**, 405 (2018).

[75] G. Wan, Y. Li, T. Lai, P. Li, Y. Zhu, J. Yang, Y.-F. Zhang, J. Pan, and S. Du, Sym4state.jl: An efficient computation package for magnetic materials, Comput. Phys. Commun. **303**, 109283 (2024).

[76] M. I. Aroyo, J. M. Perez-Mato, C. Capillas, E. Kroumova, S. Ivantchev, G. Madariaga, A. Kirov, and H. Wondratschek, Bilbao Crystallographic Server: I. Databases and crystallographic computing programs, Z. Kristallogr. - Cryst. Mater. **221**, 15 (2006).

[77] M. I. Aroyo, A. Kirov, C. Capillas, J. M. Perez-Mato, and H. Wondratschek, Bilbao Crystallographic Server. II. Representations of crystallographic point groups and space groups, Acta Cryst. A **62**, 115 (2006).

[78] G.-B. Liu, Z. Zhang, Z.-M. Yu, and Y. Yao, MSGCorep: A package for corepresentations of magnetic space groups, Comput. Phys. Commun. **288**, 108722 (2023).

[79] J. Yang, Z.-X. Liu, and C. Fang, Symmetry invariants and classes of quasiparticles in magnetically ordered systems having weak spin-orbit coupling, Nat. Commun. **15**, 10203 (2024).

[80] Y. Jiang, Z. Song, T. Zhu, Z. Fang, H. Weng, Z.-X. Liu, J. Yang, and C. Fang, Enumeration of spin-space groups: Toward a complete description of symmetries of magnetic orders, Phys. Rev. X **14**, 031039 (2024).

[81] H. Xiang, C. Lee, H.-J. Koo, X. Gong, and M.-H. Whangbo, Magnetic properties and energy-mapping analysis, Dalton Trans. **42**, 823 (2013).

[82] L. M. Sandratskii, Noncollinear magnetism in itinerant-electron systems: Theory and applications, Adv. Phys. **47**, 91 (1998).

[83] E. Bousquet, N. A. Spaldin, and K. T. Delaney, Unexpectedly large electronic contribution to linear magnetoelectricity, Phys. Rev. Lett. **106**, 107202 (2011).

[84] E. Bousquet and N. Spaldin, Induced magnetoelectric response in *Pnma* perovskites, Phys. Rev. Lett. **107**, 197603 (2011).

[85] M. Ye and D. Vanderbilt, Magnetic charges and magnetoelectricity in hexagonal rare-earth manganites and ferrites, Phys. Rev. B **92**, 035107 (2015).

[86] W. Ding, J. Zhu, Z. Wang, Y. Gao, D. Xiao, Y. Gu, Z. Zhang, and W. Zhu, Prediction of intrinsic two-dimensional ferroelectrics in In_2Se_3 and other III_2-VI_3 van der Waals materials, Nat. Commun. **8**, 14956 (2017).

[87] S. P. Beckman, X. Wang, K. M. Rabe, and D. Vanderbilt, Ideal barriers to polarization reversal and domain-wall motion in strained ferroelectric thin films, Phys. Rev. B **79**, 144124 (2009).

[88] J. Xiao, H. Zhu, Y. Wang, W. Feng, Y. Hu, A. Dasgupta, Y. Han, Y. Wang, D. A. Muller, L. W. Martin, *et al.*, Intrinsic two-dimensional ferroelectricity with dipole locking, Phys. Rev. Lett. **120**, 227601 (2018).